J. dynamic behavior mater. (2016) 2:306–325
DOI 10.1007/s40870-016-0067-1

Centrifuge Characterization of Buried, Explosive-Induced Soil Ejecta Kinematics and Crater Morphology

Curt Hansen[1] · **Ronald Y. S. Pak**[1]

Received: 18 February 2016 / Accepted: 20 April 2016 / Published online: 29 April 2016

Abstract A comprehensive experimental regime was conducted to advance the understanding of the mechanistic phenomena of buried, explosive-induced soil responses using geotechnical centrifuge modeling. To address experimental gaps in the current literature, this research documents the high-rate dynamic soil behavior under explosive loads with parametric variations of charge size, burial depth, and g-level in conjunction with post-detonation static measurement of blast-excavated craters. The novel integration of a high-speed imaging system into the centrifuge domain, placed in close proximity to the blast, enabled a rigorous in-flight characterization of the transient, multiphasic soil blast mechanics including early soil disaggregation, gas–particle interactions, and soil dome evolution. The results indicate that initial soil surface motions appear progressively later, post-detonation, with elevated acceleration. Furthermore, the data demonstrates that gravity-induced confining stresses reduce the temporal and spatial soil disaggregation flow kinematics. Crater dimensions, measured by a laser profilometer, also exhibit a gravity-dependent decrease and a new, dimensionless coupling function correlates the physical ejecta dynamics to the crater dimensional statics evident in the buried blast phenomena. An in-depth analysis compares this study's empirical scaling relationships in both dimensional and dimensionless form to a compilation of past field and centrifuge results and demonstrates their favorable correlation to full-scale explosive events. The high-fidelity, repeatable database establishes a benchmark for future parametric experimental investigations and provides a physical basis for calibration and validation of computational simulations of soil blast mechanics including soil deformation and ejecta flow.

Keywords Centrifuge modeling · Gravity scaling · Buried blast loading · High-explosives · Soil ejecta · Crater morphology

Introduction

The complex challenge to characterize the dynamic soil response under blast loading remains an on-going field of interest in applied mechanics and geotechnical engineering. Understanding explosive-induced geomaterials' behavior has diverse applications including mining and liquefaction [1, 2], planetary impacts and cratering [3–6], ground surface instabilities [7], forensic engineering [8–10], flood risk management [11, 12], and earthquake simulations [13–15]. Improvised explosive devices (IEDs) and landmines continue to present significant threats to military and civilian personnel. To develop effective predictive and preventative technologies against the harmful use of explosives, a thorough understanding of soil blast mechanics is clearly a prerequisite. Accurate and consistent experimental results are essential for both applied and theoretical progress. Consequently, many past studies have investigated explosive detonation in soil using various experimental techniques.

Field tests use large quantities of explosives and provide direct simulation of the high-rate, soil ejecta impact on overlying structures and the subsequent crater formation. For example, Ehrgott [16] fabricated a massive piston

✉ Curt Hansen
cbhansen@colorado.edu

[1] Department of Civil, Environmental, and Architectural Engineering, University of Colorado, Boulder, CO 80309-0428, USA

assembly that measured impulse generated by detonating a 2.27 kg C4 charge at surface-tangent and shallow burial depths. Bergeron et al. [17] examined the mechanisms of a mine blast event and quantified the explosive output of a 100 gram C4 charge at burial depths ranging from 0 cm to 8 cm in a small, sand-filled tank. Their flash X-ray photography provided snapshots of the early gas–soil interaction and high-speed film captured soil dome expansions. A study conducted by the US Army Corp of Engineers detonated subsurface charges ranging in size from 12 kg to 116 kg in dry and moist soils, measured the resultant apparent crater size and shape, and investigated the influence of bedrock on crater formation [18]. Drake et al. [19] compiled ground shock data from more than one hundred surface-tangent and buried explosive tests, conducted in various soils, using charges ranging from 453 grams to 1000 kg. Vortman [20] detonated 450 kg, 18,143 kg, and 453,000 kg TNT charges in desert alluvium sand and basalt rock at burial depths ranging from 2.92 m to 17.7 m. The studies cited above, with variant explosive mass, burial depths, test bed size, soil conditions, and measurement methods, reflect the general consensus: full-scale parametric studies are not feasible. These physical tests remain impractical, laborious and costly to set up, and require large quantities of explosives. In addition, the lack of control over in-situ soil conditions and the exposure to unpredictable, natural elements limits data replication and verification. Thus, parametric analysis to establish fundamental relationships by field tests are generally difficult, if not impossible. In spite of the wide variability and uncertainty in field test conditions, their test results quantify full-scale explosive yields and blast loads imparted to an overlying structure. Therefore, the data remains important to small-scale laboratory test validation and prediction of the prototype condition using scaling relationships.

Investigation by small-scale laboratory experiments at normal gravity offers more realistic parametric study through its economy and direct control of soil properties. This technique requires empirical scaling relationships, such as Sachs or Hopkinson–Cranz, to correlate between small-scale and full-scale test results. Previous works used shallow-buried, gram-sized charges and controlled test parameters to quantify pressure variations above a soil blast and also blast impulse imparted to above-surface target plates using Hopkinson–Cranz scaling relationships [21–23]. However, Hopkinson–Cranz scaling relationships assume gravitational influence on the soil overburden to be negligible. Because geomaterials' behavior strongly depends on the stress level, the model-scale tests' parametric exclusion of gravity generally limits this technique's applicability to air-blast or shallow burial depths. As a result, this approach typically omits the key stress similitude requirement in soil mechanics.

To overcome this critical stress similitude issue, the centrifuge scaled modeling technique has proved to be a practical and versatile solution for small-scale laboratory experiments in geomechanics and geotechnical engineering. It permits realistic simulations of full-scale, nonlinear geotechnical problems by reproducing gravity-induced stress levels that dictate the mechanics of the soil's response under blast loading. With suitable scaling relationships between scaled model and prototype conditions, a much smaller soil model size and amount of explosive mass can produce stresses and deformation characteristics comparable to full-scale blast events. The controlled and replicable test conditions improve test efficiency, data accuracy, extrapolation to prototype conditions, and thus enable in-depth parametric studies.

An early Soviet experimental study investigated the cratering process using buried charges within an accelerated reference frame and demonstrated that as gravity increased, apparent crater dimensions decreased, as cited in Johnson et al. [24]. Credited with first recognizing gravity's significance to blast-induced crater morphology, Chabai [25] derived a set of scaling relationships by dimensional analysis inclusive of physical variables such as charge burial depth, gravity field strength, and explosive energy. Furthermore, Johnson et al. [24] investigated crater dependence on gravity by subjecting the soil model, installed on an aircraft, to accelerations from 0.17 g to 2.5 g's. This study reported that subsequent small-scale charge detonations, apparent crater dimensions varied inversely to g-field for all burial depths considered.

Most of the initial centrifuge soil blast studies investigated the impact of increased g-level on crater formation using surface-tangent or shallow-buried explosives, emphasizing soil conditions, charge properties, and gravity level as determinant factors in apparent crater dimensions [8, 26–31]. Schmidt and Holsapple [26, 27] extensively examined the effects of elevated acceleration on the explosive cratering phenomena and substantiated that crater size remains gravity-dependent. Their experimental program used half-buried, gram-size charges detonated in small, cylindrical containers of dry Ottawa sand and subjected to gravity levels predominantly greater than 300 g's. Furthermore, the similarity analysis derived dimensionless Π groups relating the crater volume, radius, and depth to the g-level, soil properties, and explosive characteristics. Their experimental results evidenced that small charge detonation at increased acceleration can simulate large explosive yields by centrifuge scaled modeling, and thus demonstrated the relevance of this technique. And finally, confirmed by on-board imaging and crater axial symmetry, their data showed that craters formed in the Ottawa sand remained stable, unaffected by ambient vibrations or air flow during centrifuge spinning. Goodings et al. [28]

reported similar findings, specifically the absence of undesirable acceleration related scale effects at lower g-levels (31–100 g, the range typical of most geotechnical centrifuges).

As a result, centrifuge modeling offered potential application to extended fields of research. For example, a study by Brownell and Charlie [29] determined that the soil's moistures content significantly impacted crater dimensions due to the matric suction in partially saturated soil. In addition, Kutter et al. [8] applied the centrifuge modeling technique to study the explosive response of scaled tunnel models to buried gram-size charges. Gill and Kuennen [30] developed a transparent specimen container that allowed cross-sectional viewing of the blast event under elevated gravity and used a cinema camera and electronic imaging system to capture soil displacement data. However, the limitations of their photographic techniques precluded the recovery of useable displacement data. Therefore, real-time, sequential imagining of soil ejecta displacements and velocity time-histories were not obtained. The work reported by Shim [31] examined the dynamic response of saturated soil under blast loading in the free-field condition and also the soil–structure interaction problem using a model pile embedded in sand at equivalent prototype conditions. An analog camera and tape recorder captured only limited, segmented sequences of the explosive event. Measurements of excavated craters entailed imprinting the apparent crater using a gypsum-water mixture, measuring the radius and diameter of the cured mold, and finally submerging the crater mold in water to measure water displacement in order to estimate the volume of soil heaved. The study adhered to a single prototype condition, which precluded an analysis of increased artificial acceleration's impact on ground motions and apparent crater formation as a function of varying charge explosive weight and burial depth. Clearly, the need exists to better characterize the centrifuge in-flight dynamic response of a particulate medium when subjected to explosive loading, the focus of this research.

This paper presents an innovative experimental program that examines the mechanistic phenomena of buried explosive-induced soil responses using centrifuge scaled modeling. The explosive tests were conducted on the 400 g-ton, 6 m radius geotechnical centrifuge at the University of Colorado, Boulder. To delineate gravity-field influence on soil ejecta flow and crater dimensions, specific to fully-buried explosives, the parametric investigation includes various gram-sized charges embedded into a large, dry natural soil model at different burial depths and detonated at multiple g-levels. This research seeks to accurately measure soil ejecta kinematics and crater morphology by developing novel measurement techniques that integrate state-of-the-art technologies into the experimental regime. The high-speed imaging system placed into the centrifuge domain, in close proximity to the blast, captured the transient, multiphasic, soil blast mechanics typical of a buried, full-scale explosive detonation. As discussed above, past studies have confirmed that small-scale laboratory tests at elevated gravity can simulate large-scale field test data by using the conventional cube-root or dimensionless Π groups scaling relationships [8, 25, 27, 28, 32]. An in-depth analysis of the centrifuge scaling relationships, presented in the following sections, compares this study's empirical relationships in both dimensional and dimensionless form to past field and centrifuge results and demonstrates their correlation to and prediction of full-scale explosive conditions. The results further substantiate that small charge detonation at increased acceleration can simulate and predict large explosive yields by centrifuge scaled modeling. The significant experimental database allows parametric calibration and validation of computational codes that simulate iterative configurations of soil blast mechanics in prototype scale.

Experimental Technique

In order to integrate the advanced instrumentation into the centrifuge domain and to physically simulate a half-space condition, a large, rectangular steel container was fabricated with planar dimensions of 1.2 m by 1.0 m, and a height of 0.61 m. Stress wave absorbing panels, composed of viscous, oil-based putty known as Ductseal, lined the soil container's walls to mitigate incident wave reflections and dynamic boundary effects present in a finite domain [33–35]. The soil stratum configuration consisted of dry, Colorado Mason sand classified as a cohesionless, poorly-graded sand (SP), with a specific gravity of 2.62 [36, 37]. A sieve analysis on the soil confirmed a diverse particle size distribution: particle diameters ranged from 200 to 3000 μm, as depicted in Fig. 1. Preparation of the soil model by pulviation yielded a uniform dry density of 1735 kg/m^3, correlating to a relative density of 88 % and a void ratio of 0.54. A chosen soil depth of 0.29 m resulted in width-to-depth and length-to-depth ratios of 3.1 and 3.8, respectively.

Centrifuge scaling relationships enable small, gram-sized charges to simulate blast energy typical of a full-scale, explosive field test, by scaling the explosive mass (N^3) as model charges accelerate to Ng [26–28, 32]. For example, a 1 gram model charge accelerated to 50 g's simulates a 0.14 ton explosive in the field at prototype scale. This study used three different sizes of pentaerythritol-tetranitrate (PETN) and RDX-based exploding bridgewire detonators (EBWs), manufactured by Teledyne Reynolds, which functioned either as primary explosives or

secondary initiating detonators: RP-87, RP-80, and RP-81 with respective explosive masses, 69 mg, 203 mg, and 530 mg. Additionally, this study used composite cylindrical charges synthesized with 880 mg plastic explosive Composition C4 (91 % RDX, 9 % plasticizer) coupled with a RP-80 detonator, consistently resulting in a total explosive mass of 1000 mg within a ±0.1 % accuracy, an average density of 1.57 gm/cm^3 and an aspect ratio of 1.05. Digital calipers verified the precise depth of burial (DOB), measured from the soil surface to the distal end of the charge. The DOBs varied with a majority of tests conducted at burial depths: 2.5 cm; 5.1 cm; and 7.6 cm. Due to the inherent directionality of EBWs, the explosive was placed with its longitudinal axis oriented vertically and its distal end nearest to the soil surface.

The high-speed imaging system included the following interactive components: a color CMOS sensor v710 Vision Research Phantom high-speed camera; high-intensity, white-light emitting diodes (LED) flood bars; and two optically flat mirrors (Fig. 2).

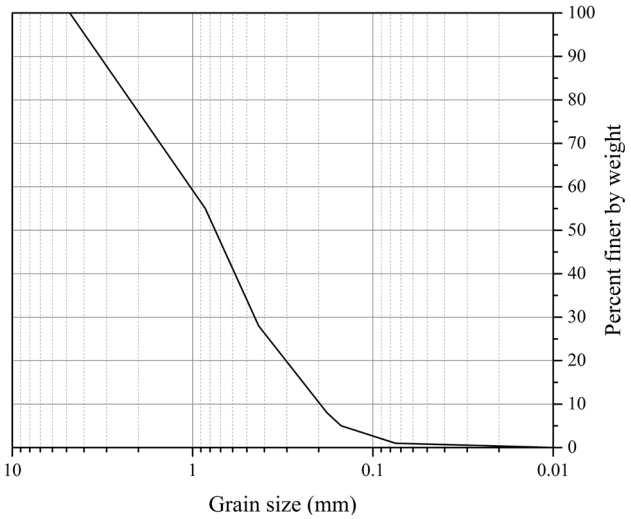

Fig. 1 Particle size distribution for Colorado Mason sand

The high-speed video camera captured sequentially, in real-time, the early expansion of detonation gas products in addition to soil heave evolution and particle trajectories under accelerated gravity. The camera outfitted with an acrylic protective screen and particulate filters recorded blast images at 41,013 frames per second (fps) and 4 μs shutter speed. The use of a color high-speed camera delineated the diverse shades of soil particles existent in Mason sand and the subsequent multi-dimensional, visual image improved particle tracking. The high-speed video camera, fitted with the wide-angle lens, was mounted on a support channel suspended directly over the buried charge at a calculated distance of 56 cm above the soil surface to avoid potential damage and vibrations induced by soil blast loading (Figs. 2, 3). The camera's unique location required the specular reflection of the blast image from the two mirrors. The mirrors, bolted to the soil container's sides and oriented 90° relative to one another, maintain an equal angle of incidence and reflection, and thereby establish a horizontal, ground-surface view of soil ejecta. A Berkeley Nucleonics Corp. digital pulse generator synchronized and triggered all electrical components including the Reynolds FS-43 Fire Set and the high-speed imaging system. Centrifuge operation during a soil blast test entailed spinning the centrifuge to the prescribed g-level, detonation of the charge, and decelerating the centrifuge to a complete stop. Video surveillance in the centrifuge pit, in addition to a small digital camera mounted on the soil container, provided continuous monitoring of the experiment during flight.

Next, post-test static measurements and photographs ensued, designed to supplement real-time data collection. After each detonation, a line gage and digital calipers extracted crater dimensions. In later test series, a LMI Gocator surface laser system generated 3-D profiles of excavated craters with improved precision and efficiency over point-wise contact methods. Then, the analysis of 400–1000 high-speed video frames, using the proprietary software distributed by Vision Research, extracted a corresponding number of data points specific to each g-level

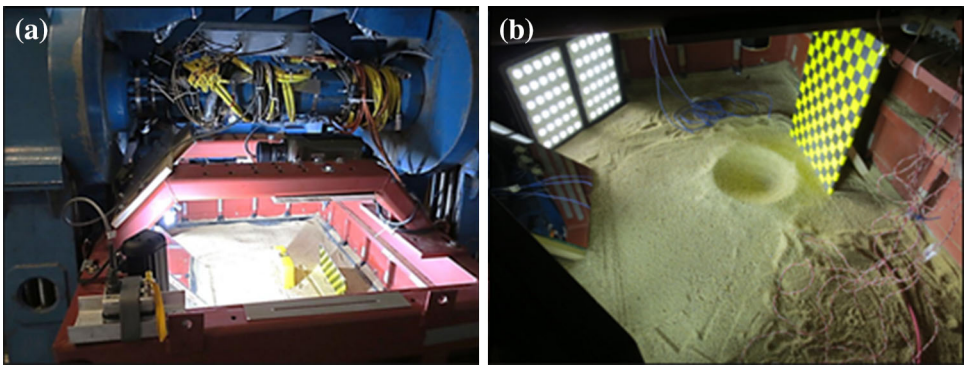

Fig. 2 **a** Soil container and integrated components on 400 g ton centrifuge at UCB. **b** In-box perspective

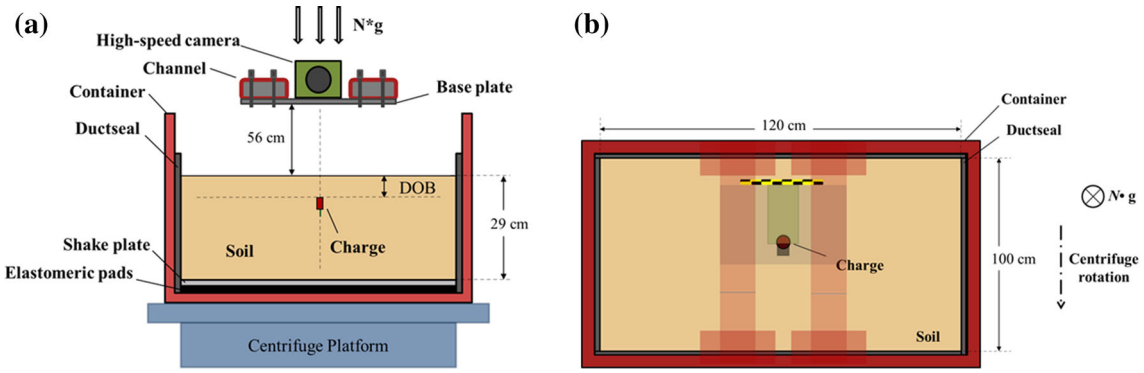

Fig. 3 Schematics of experimental layout for buried soil blast tests on the centrifuge. **a** *Side*-view; **b** *top*-view (overlying camera and supportive cross-channels semi-transparent). Rotational trajectories and gravity vectors are shown. *Note*: **a** and **b** are not to scale

test. The motion analysis software, a two-dimensional particle tracking program, first requires the calibration of the digital image reference scale (unit length/pixel) in-plane relative to the buried explosive. Next, a prescribed origin set at the soil-air interface defines the x–y coordinate system. The user selects a search area of interest, i.e. initial soil deformation, that encompasses the first tracked point and the software subsequently detects the linear translation of the particle in sequential images. This in turn, quantifies the temporal and spatial soil ejecta heave.

Experimental Results

Soil Ejecta Kinematics

The key experimental results from over 50 explosive tests and their analytical synthesizes are presented in the following sections. Standard earth gravity tests included in the results augment data analysis and clarify the influence of increased gravitational forcing.

The following analysis provides critical qualitative insights into the highly transient, multi-phase soil blast mechanisms. This test series used a 1 gram C4 charge, under a 5.1 cm soil overburden, and detonated at 4 g-levels (1 g, 20 g, 30 g, and 40 g), with model burial depths scaling to 0.051 m, 1.0 m, 1.5 m, and 2.0 m in prototype condition. The video sequences, at coincident millisecond intervals, effectively illustrate the gravity-induced stress-level impact on the buried blast phenomena (Fig. 4).

The initial ground motions at the soil-air interface, measured by high-speed video, occurred approximately 0.214 ms post-detonation at the 1 g-level. The consequent soil surface motions appear progressively later with increased gravity: 0.415 ms at 20 g; 0.595 ms at 30 g; and finally, 0.710 ms at 40 g. It is evident that the arrival of the shock wave and pressurized gases at the soil surface lengthen with elevated gravity-induced stress levels, and thus soil ejecta displacements occur later.

As illustrated in Fig. 4a, the first row of high-speed video frames, recorded at 2.85 ms, reveals the opaque gas detonation products jetting through the soil at each tested g-level. This specific frame illustrates the early thermodynamic phase of a buried blast event: the immediate gas–soil particle interaction. In this stage, the heat transfer mechanism crushes and even pulverizes the soil adjacent to the charge as the shock wave passes through the soil material [17]. The pressurized gases and shock wave impart kinetic energy into the particulate medium causing the soil matrix to collapse followed by soil deformation at the surface as observed in Fig. 4. Next, the explosive gases expand radially and initially jet past the soil cap domain, creating a dilute suspension of particles dragged upward with the detonation products, visually evidenced in Fig. 4, especially at lower g-levels. The continuous radiating pressure impulse drives overlying soil into the air, eventually penetrating the expansive gas bubble, encasing the detonation products in a soil annulus (Fig. 4). Then, both constituents (gas and soil) swell and rapidly accelerate in a predominantly vertical direction due to lateral soil confinement, with relatively uniform, hemispherical mound growth. This observed trend continues in the early stages of the blast event in all four tests (Fig. 4a–c).

As illustrated by the video frames for the different g-levels, it is evident that elevated gravity, which led to heavier overburden loads at a constant burial depth, significantly impacts the buried blast phenomena. A closer examination of the video frames at 1 g shows a radial soil dome expansion, typical of the inverse cone (Fig. 4a–c, 1 g). In contrast, the high-speed video frames at the 40 g-level depict a slightly asymmetrical, vertical directionality that dominates soil dome heave with increased gravity (Fig. 4d). Here, the soil dome heave exhibits less uniformity in surface contours, with a pointed apex and sloping,

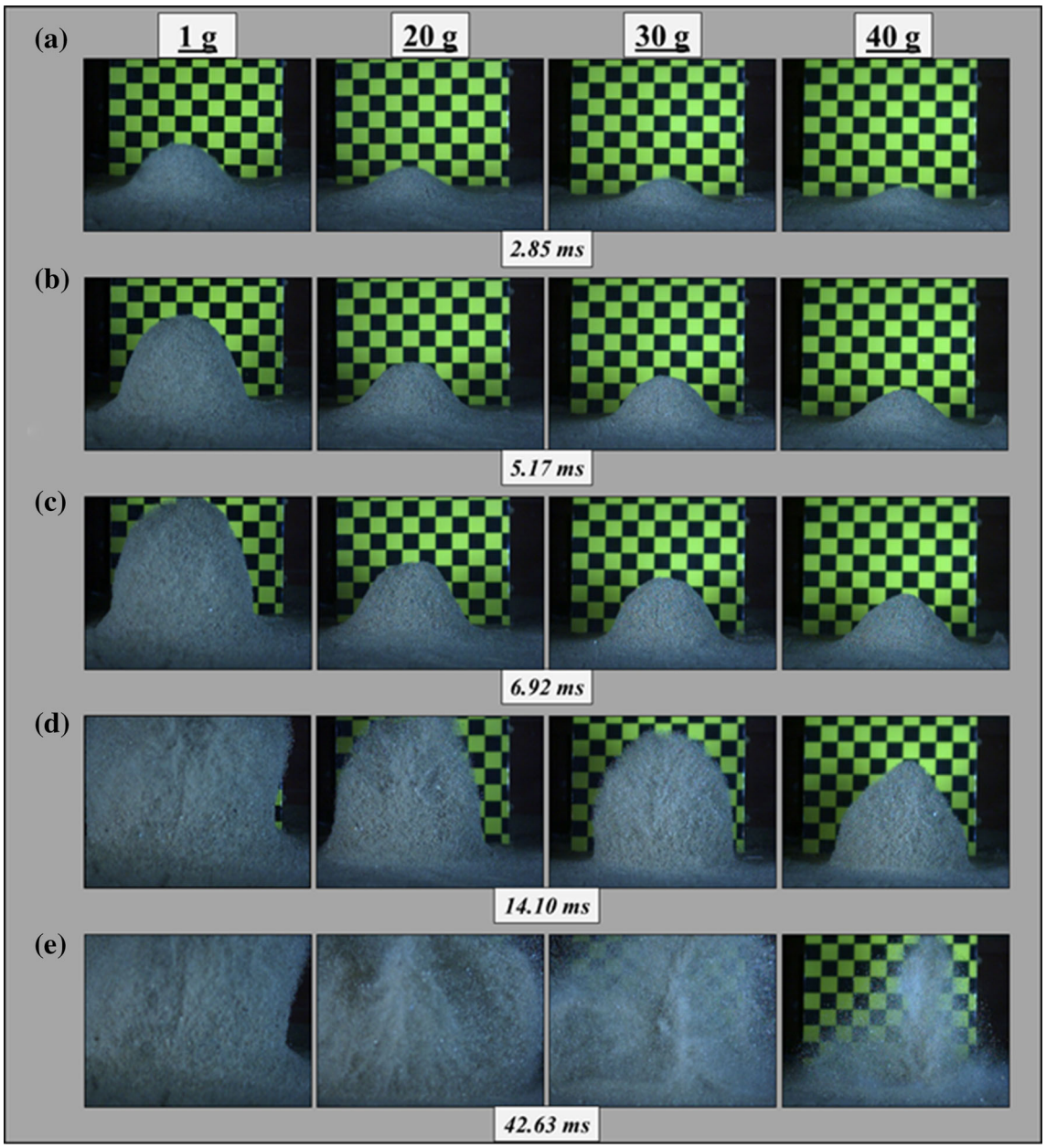

Fig. 4 Comparison of soil deformations for 1 gram C4 charge detonated at 5.1 cm burial depth and corresponding gravitational accelerations: 1 g (*left*), 20 g (*left center*), 30 g (*right center*), and 40 g (*right*). Time after detonation: **a** 2.85 ms; **b** 5.17 ms; **c** 6.92 ms; **d** 14.10 ms; **e** 42.63 ms. Fiducial background 2.2 cm *square* grid in length

asymmetric sides. This can attribute to the gravity-induced increase in overburden pressure which restricts the radial flow of the detonation products and soil ejecta. The same mechanism also appears to inhibit soil mound diameter dimensions (Fig. 4d, 40 g).

Clearly apparent, the soil dome expansion rate decreases with increased g-level. As witnessed in the 1 g test, the propagating soil dome reaches the upper boundary of the camera's high-speed image frame at 6.92 ms after detonation, preceding the 40 g, 30 g, and 20 g-level tests by 17.53 ms, 10.29 ms, and 6.17 ms, respectively, a significant difference within the milliseconds time sequence of the entire blast event (Fig. 4c). Furthermore, the soil dome heave at 1 g displays the early venting (Rayleigh–Taylor instability [38]) and soil mound disassociation in the upper portion of the gas bubble at 14.10 ms, followed by the soil fall-back to form the excavated crater, as shown in the following image (Fig. 4d). In contrast, at the 40 g-level, in the relatively, late-time lapse, 42.63 ms (Fig. 4e), the soil ejecta only begins to deposit in and around the plastically deformed crater wall. In addition, this specific frame depicts thin jets

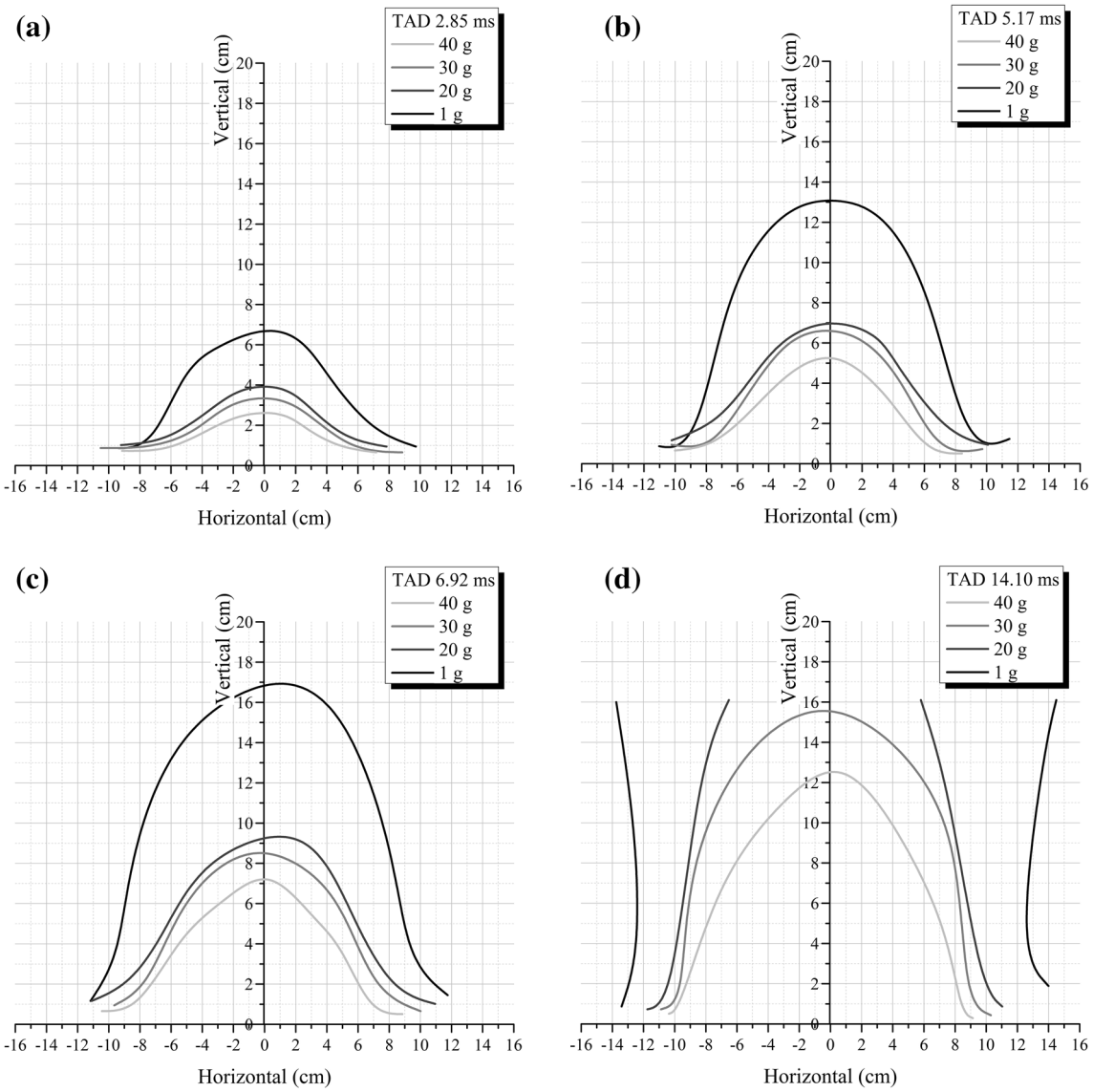

Fig. 5 Sequential soil dome profiles as a function of time after detonation (TAD): **a** 2.85 ms; **b** 5.17 ms; **c** 6.92 ms; **d** 14.10 ms; for a 1 gram charge buried 5.1 cm and detonated at the 40 g, 30 g, 20 g, and 1 g-level

of detonation products finally extruding through the stiffened soil matrix. This observation suggests that the higher effective gravity-induced soil stress proximate the charge suppresses early soil mound dissociation and confines detonation products for a longer time period when compared to lower g-levels.

Blast-excavated crater and outer ejecta lip formation at 40 g occurs 82.05 ms post-detonation. In comparison, the same phenomena occurs at the 30 g and 20 g-level. However, the decreased gravity-induced stresses slow down final crater formation to 121.20 ms and 164.75 ms, respectively, a significant time increase of 39.20 ms and 82.70 ms. And finally, in the 1 g test, most of the soil ejecta continues to propagate radially in the late stages of the explosion beyond the field of view (Fig. 4e, 1 g).

Because the fundamental physics of an explosive event do not change with explosive mass [39], these highly resolved, rate-dependent, sequential images of the complex, interactive soil blast mechanisms simulate the same phenomenon apparent in full-scale field tests. These results provide a sound physical characterization of the actual dynamic material behavior under buried blast loading with identification of initial soil deformations and consequent temporal and spatial ejecta flow.

Quantification of Soil Ejecta Flow

The high-speed videos combined with motion analysis software, developed by Vision Research [40], and discussed

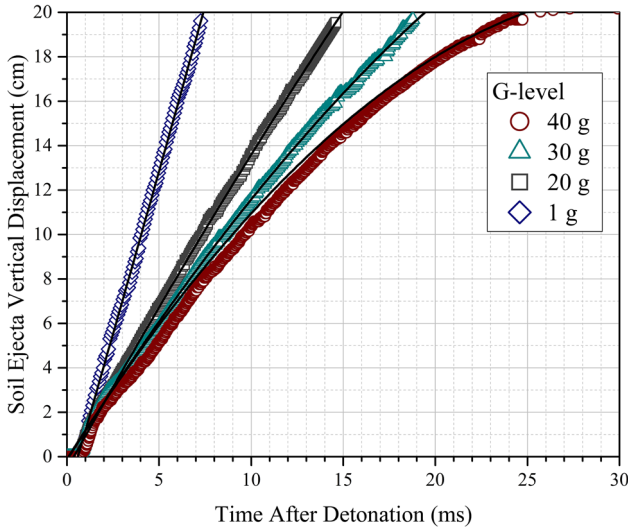

Fig. 6 Time growth of soil dome ejecta vertical height for a 1 g charge buried 5.1 cm and detonated at the 1, 20, 30, and 40 g level. The *vertical* field of view extends to 20 cm. Parabolic best-fit regression lines included (*solid lines*)

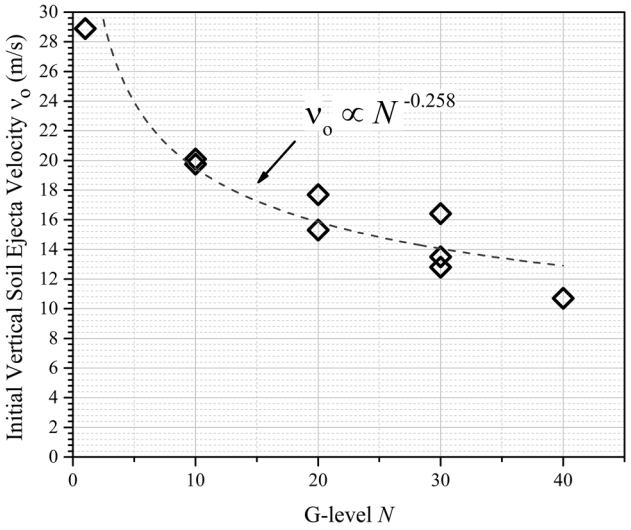

Fig. 7 Initial *vertical* soil ejecta velocities as a function of g-level for a 1 gram charge buried 5.1 cm. Included power-law regression fit (*dashed-line*). Coefficient of determination (R^2) measured 0.849

in methods, extracted rate-dependent displacement data and quantifies soil ejecta kinematics. The soil dome profiles at the same early millisecond intervals shown in Fig. 5 quantify the previously observed gravity-dependent soil ejecta distribution trends illustrated in Fig. 4. The data substantiates that increased soil overburden induced by elevated gravity significantly reduces the soil dome spatial expansion rate (Fig. 5a–d). Also, the vertical, asymmetrical directionality evident at higher g-levels, distinctly contrasts to the 1 g profile (Fig. 5d). And finally, as evidenced in the comparison plots, gravity restricts the radial flow of soil ejecta and therefore inhibits soil mound dimensions.

Further data analysis determined the vertical soil dome ejecta height as a function of time post-detonation at the tested g-levels (Fig. 6). In general, the displacement time-history plots adhere reasonably well to a linear regression throughout the examined range. Each linear regression line correlates to a range of 400–1000 data points specific to each g-level (Fig. 6).

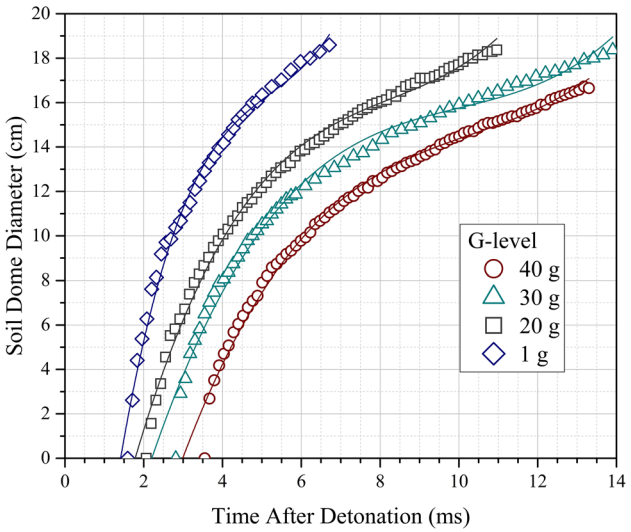

Fig. 8 Time evolution of soil dome width for 1 gram charge detonated 5.1 cm and corresponding accelerations: 1 g, 20 g, 30 g, and 40 g. Included cubic-polynomial regression fit (*solid line*)

Table 1 Summary of vertical soil ejecta velocities for 1 gram charge buried 5.1 cm and detonated at various g-levels

G-level *N*	DOB	Initial ejecta motion (m/s)	Initial vertical ejecta velocity ($h = 8$ cm) (m/s)	Mean vertical ejecta velocity ($h = 20$ cm) (m/s)
1	5.1	0.214	28.9	26.5
10	5.1	0.300	21.2	20.3
20	5.1	0.415	15.3	14.4
30	5.1	0.595	13.5	10.4
40	5.1	0.710	10.7	9.8

Table 2 Summary of soil ejecta dome diameters and flow angles for 1 gram charge buried 5.1 cm and detonated at the 1 g, 20 g, 30 g, and 40 g-level

G-level N	DOB (cm)	Soil dome diameter d (cm)						Soil dome ejecta angle θ (°)				
		d(t = 6.7 ms) (cm)	d_0 (m/s)	d(t), θ(t) = $A + B_1t + B_2t^2 + B_3t^3$								θ(t = 14.7 ms) (°)
				A	B_1	B_2	B_3	A	B_1	B_2	B_3	
1	5.1	18.6	106.2	−19.83	18.20	−3.24	0.21	165.80	−15.02	0.85	−0.02	79.5
20	5.1	14.5	81.3	−13.62	9.38	−1.05	0.04	188.99	−17.12	1.05	−0.02	93.5
30	5.1	13.1	58.0	−14.62	8.22	−0.78	0.03	175.94	−11.93	0.57	−0.01	94.1
40	5.1	11.1	39.1	−19.83	8.77	−0.79	0.03	172.56	−7.88	0.13	0.00	96.5

d_o = initial soil ejecta diameter expansion rate

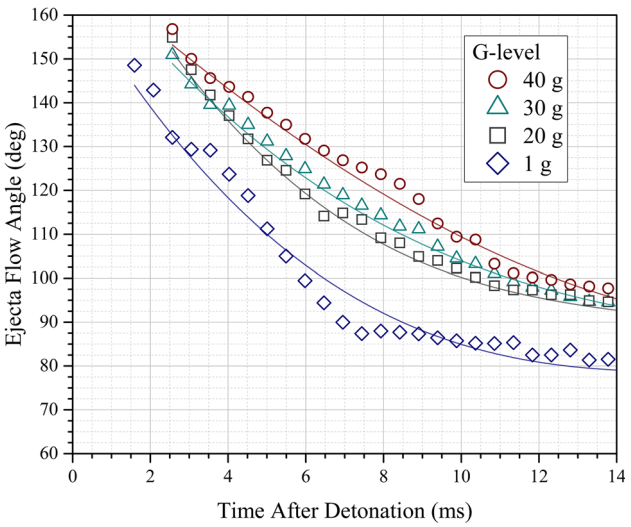

Fig. 9 Time evolution of soil ejecta flow angle for 1 gram charge detonated 5.1 cm and corresponding accelerations: 1 g, 20 g, 30 g, and 40 g. Included cubic-polynomial regression fit (*solid line*)

The highly-resolved time-history plot shows that vertical soil ejecta velocities decelerate with elevated g-level (Fig. 6), yielding a speed of 28.9 m/s at 1 g and declining to 10.7 m/s at 40 g. As the lithostatic pressure increases with g-level, more explosive energy propagates through the soil skeleton rather than dispersing to the air [28]. The stiffened soil matrix confines detonation gas expansion, delays disaggregation, and progressively attenuates soil ejecta momentum with consequent deceleration of vertical velocities, clearly observed at 40 g by the downward parabolic profile. Table 1 summarizes initial ejecta motion in addition to initial and mean vertical soil ejecta velocities. The slope of a linear curve fit to the displacement data (Fig. 6) over the first 8 and 20 cm defines the initial and mean vertical ejecta velocities, respectively.

The initial time of soil motion (t_o) gravity-dependence approximated by the empirical equation

$$t_o = 0.204 + 0.006N^{1.195} \quad (1)$$

indicates a nonlinear increase in initial soil surface spallation under elevated g-level, or overburden pressure. Also, a linear regression analysis determined that initial vertical soil ejecta velocities v_o best fit a power-law dependence on g-level as shown in Fig. 7.

The derived relationship between initial vertical ejecta velocities and gravity forcing is

$$\mathbf{v_o} \propto \mathbf{N}^{-0.258} \quad (2)$$

and evidences that initial vertical soil ejecta velocities display a nonlinear reduction at subsequent higher gravity-induced stress levels. The data shows a significant decrease between the 1 and 10 g-levels, followed by a gradual asymptotic decline. Furthermore, the initial vertical ejecta velocities decrease by more than 50 % at the 40 g-level relative to the 1 g-level, a difference strongly attributed to the increased shear resistance of cohesionless soil to deformations under elevated gravity.

To further characterize the soil dome ejecta front, the results quantify soil dome diameters and ejecta flow angles,

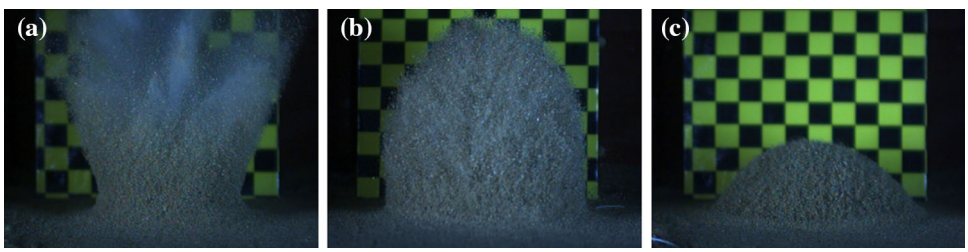

Fig. 10 Comparison of soil deformations for 1 gram charge detonated at the 30 g-level and buried **a** 2.5 cm (TAD = 2.93 ms); **b** 5.1 cm (TAD = 16.4 ms); and **c** 7.6 cm (TAD = 23.7 ms)

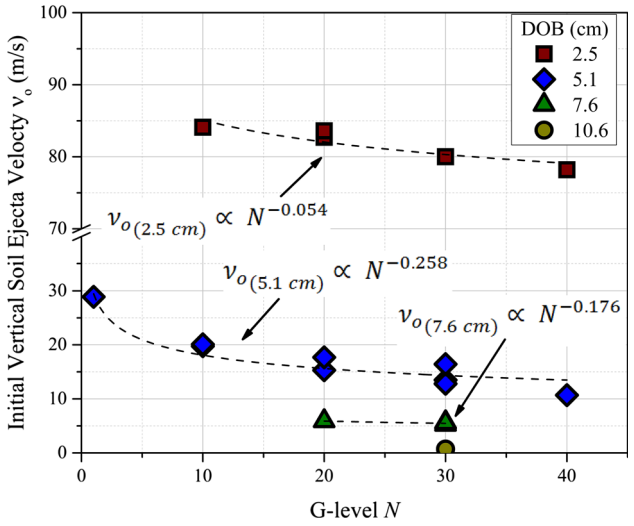

Fig. 11 Initial vertical soil ejecta velocities versus g-level for 1 gram charge buried 2.5 cm, 5.1 cm, 7.6 cm, and 10.6 cm and detonated at multiple gravity levels. Initial vertical soil ejecta velocities derived by linear regression fit (*dashed line*) to temporal evolution of vertical soil ejecta displacement over 3 ms interval

Table 3 Mean initial vertical soil ejecta velocities as a function of burial depth (DOB) and g-level for a 1 gram charge detonation

G-level	Burial depth (cm)			
	2.5	5.1	7.6	10.6
1		28.9		
10	84.1	21.1		
20	83.6	15.3	5.9	
30	80.0	13.5	5.5	0.1
40	78.2	10.7		

Inset mean initial vertical soil ejecta velocity values have units of m/s

as presented in the following discussion. To be consistent, an arbitrary datum 3.8 cm above the soil surface functioned as the horizontal reference to measure the lateral dimension, or soil dome diameter. The included angle between the plane tangent to the soil heave at the 3.8 cm datum and the horizontal denotes the ejecta flow angle. Figure 8 illustrates the effect of gravity on the temporal evolution of the soil dome diameter.

As anticipated, the results substantiate a similar gravity-dependent trend: soil dome diameter dimensions decrease with elevated g-level and dilate at a reduced rate (Fig. 8). The gravity-induced confining stresses strongly impede the lateral expansion rate of soil disaggregates with subsequent vertical directionality typical at higher centrifuge acceleration. This contrasts to the rapid, horizontal growth evidenced at 1 g. Specifically, the evolving soil dome diameter at 1 g measured 18.6 cm at the earliest time, 6.71 ms post-detonation. Soil dome diameter dimensions at the tested g-levels are summarized in Table 2. Furthermore, an analysis of the initial slopes of the curves, determined by linear regression, indicates that as time increases, soil dome diameter displacements decrease and reasonably adhere to a cubic fit (Fig. 8).

A closer investigation of the ejecta flow field reveals that gravity plays a formative role in the time-dependent ejecta flow angle (Fig. 9).

The ejecta flow angles specific to the various centrifugal accelerations (and cubic polynomial-fit parameters) are listed in Table 2. The percent change between 1 and 40 g shows the greatest increase of 21.5 % in the included ejecta angle. At first, the 1 g soil dome heave exhibits rapid radial expansion with eventual soil ejecta flow typical of the inverse cone (Fig. 4d, 1 g) and an included angle of 79.5° (Table 2). Gravity-induced confining stresses slow down the expansion rate of the detonation gases and restricts radial flow of ejecta, redirecting the blast momentum in the upward, vertical direction (Fig. 4d, 20 g, 30 g, 40 g) with resultant angular increases (Table 2). The blast momentum decays, and hence soil ejecta flow angles at elevated gravity approach a horizontal asymptote near 94° at 12 ms.

Burial Depth Effects on Ejecta Rheology

To gain insight into the burial depth impact on disaggregation flow kinematics, a comparison of high-speed video images at three different burial depths (2.5 cm, 5.1 cm, and 7.6 cm) and a constant 30 g-level, are shown in Fig. 10. Clearly apparent, soil dome heave expansion rates decrease significantly as burial depth increases.

The pronounced interaction of jetting gas-products (Rayleigh–Taylor instability) and soil particulates appear significantly sooner at 2.93 ms after detonation for the shallowest 2.5 cm burial depth (Fig. 10a). In contrast, at the 5.1 cm and 7.6 cm burial depths, the soil ejecta confines the expanding gas products within an annulus at the later times 16.4 ms and 23.7 ms post-detonation, respectively (Fig. 10b, c). Also noteworthy, the soil disaggregation and ejecta distribution observed at the 2.5 cm burial depth appears highly irregular and stochastic when compared to the deeper burial depths. At the 5.1 cm and 7.6 cm DOB, the soil dome heaves exhibit a more uniform, hemispherical contour and pronounced asymmetric, vertical flow directionality. In contrast, the ejecta flow field evidenced in the shallowest detonation (Fig. 10a) exemplifies the classic inverted cone profile. These same *burial depth* dependent trends correlate to the previously discussed *gravity* dependent trends (Fig. 4).

To further characterize the soil ejecta rheology and to differentiate between gravity and depth of detonation effects, initial vertical soil ejecta velocities are examined

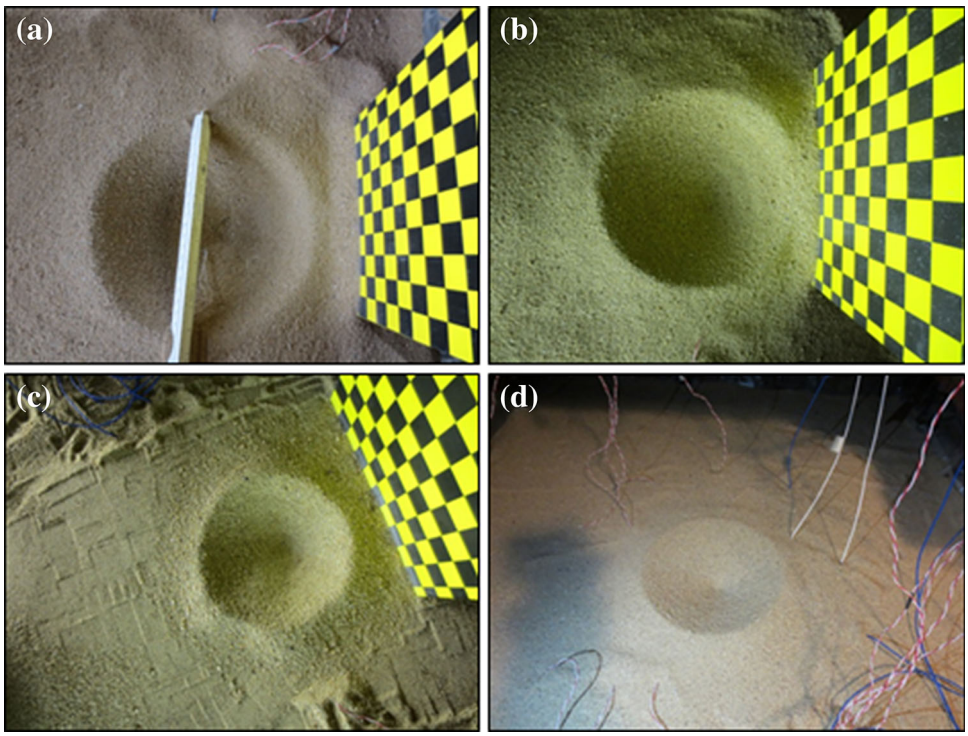

Fig. 12 Top view of blast-excavated final craters for 1 gram charge buried 5.1 cm and detonated at g-levels: **a** 1 g; **b** 20 g; **c** 40 g; **d** 50 g

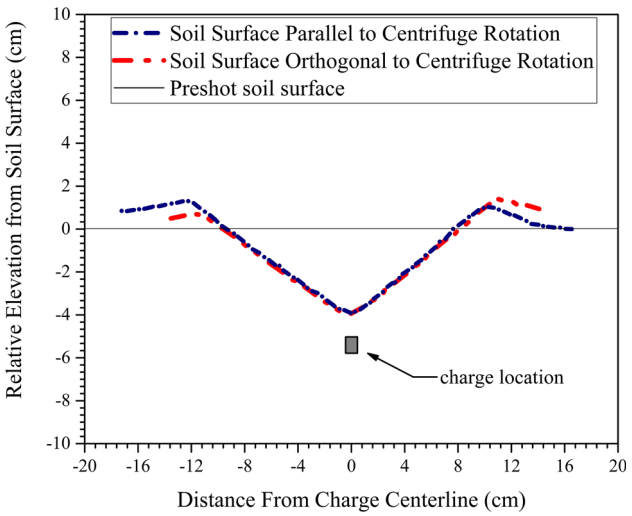

Fig. 13 Cross-sectional scan employing laser line profilometry of a final crater subsequent 1 gram charge buried 5.1 cm and detonated at the 50 g-level

for a 1 gram charge as a function of both test parameters (Fig. 11).

As discussed previously, the initial vertical soil ejecta velocities decline as a function of increased g-level for a 1 g charge buried at 5.1 cm and best fit a power-law model (Fig. 7). A comparison of the 5.1 cm results to the 2.5 cm and 7.6 cm DOB data sets exhibits the same trend: initial vertical soil ejecta velocities gradually decrease as a function of increased g-level independent of burial depth (Fig. 11). A regression analysis determined the initial vertical soil ejecta velocity gravity-dependence at the 2.5 cm and 7.6 cm DOBs, are approximated by the following equations:

$$v_o(DOB = 2.5\ cm) \propto N^{-0.054} \quad (3)$$

$$v_o(DOB = 7.6\ cm) \propto N^{-0.176} \quad (4)$$

Furthermore, at the 10.6 cm burial depth and 30 g-level, the in situ vertical stress level, comparable to a 0.32 m depth at normal gravity, results in the complete confinement of the blast phenomenon with minimal surface spallation. In this case, the explosion transmits kinetic energy to the soil matrix and forms a camouflet, encompassed by pulverized grains and highly-compressed soil. Table 3 summarizes mean initial vertical soil ejecta velocities for a 1 gram charge as a function of burial depth at varying g-levels.

As expected, the results substantiate that shallow-buried charges consistently induce higher initial vertical soil ejecta velocities compared to deeper burial depths for all g-levels tested. Within the data sets, the results evidence less variance as a function of g-level and fixed DOB when compared to the significant difference in ejecta velocities between data sets for a constant g-level and varied DOB. Here, the data confirms the trend that initial vertical soil ejecta velocities decrease as a function of increased g-level, independent of burial depth. The data also shows that gravity's impact on initial vertical ejecta velocities remains

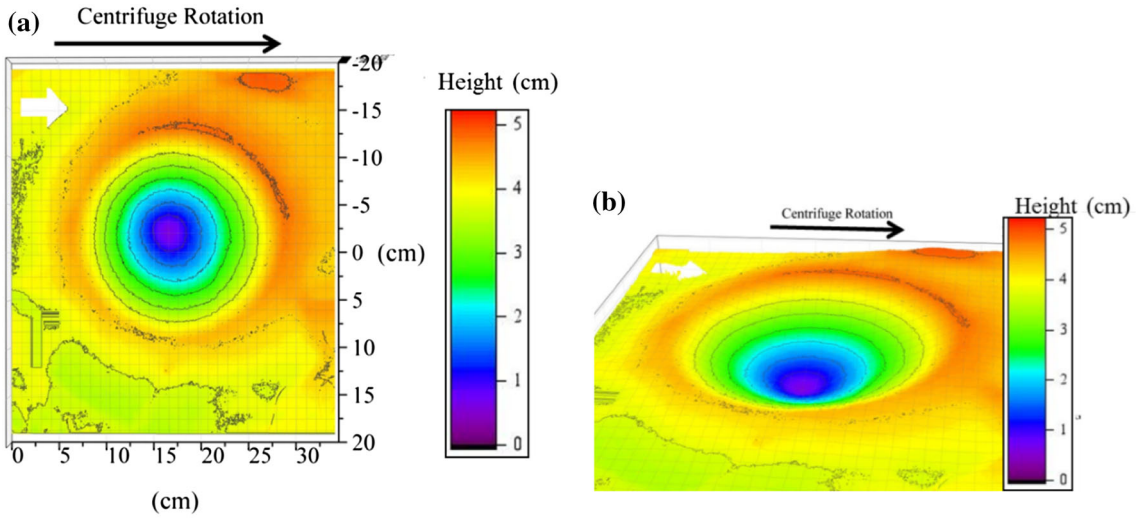

Fig. 14 Measurement scans employing laser line profilometry of a final crater subsequent 1 gram charge buried 5.1 cm and detonated at the 50 g-level. Views: **a** perspective from axis of centrifuge rotation in-flight; **b** oblique. *Arrow* points towards the direction of laser travel and centrifuge rotation

less significant when compared to burial depth effects in the tested g-level range.

Crater Morphology

The experimental results of multiple test series clarify gravity's influence on the cratering phenomenon. Blast-excavated crater morphology strongly depends on soil overburden pressure, explosive energy released, and in-situ soil cohesion and strength. Soil ejecta fallback, soil density, burial depth, and charge orientation constitute second-order effects on the final crater. Figure 12 effectively illustrates the gravity, or soil confinement, effects on blast-excavated cratering for a constant charge size (1 gram) and burial depth (5.1 cm) at 1 g, 20 g, 40 g, and 50 g-levels.

The crater profiles illustrate that peak crater dimensions occur at 1 g and decline with increased gravity imposed overburden stress. All the observed final craters shown in Fig. 12a–d resemble inverted right cone geometries and consistently maintain that shape throughout each test, independent of g-level. The observed dimensional changes in crater formation, as a function of gravity, can attribute to the in-situ variation of gravity-induced shear resistance in dry soils.

The LMI Gocator surface profilometer representative laser measurement scans (1280 points/line) as shown in Fig. 13 correspond to a specific test delineated above (1 gram, 5.1 cm DOB, 50 g; (Fig. 12d)).

The consequent final crater outlines display a distinct v-shape, hyperbolic profile with a slightly rounded apex. By superimposing the scans of the cross-sectional splices, one imaged parallel and the other orthogonal to the direction of centrifuge rotation, the two crater profiles show minimal variation only in the crater lip region. The slight horizontal skewness between the two profiles varied nominally 8.4 mm. The difference between the crater lip heights varied by only 2.7 mm. The congruent final crater included angles both measured 66.3° at 50 g's. The coincident profiles strongly convey axisymmetric final craters.

Furthermore, cross-sectional profiles captured at 51 µm intervals along the profilometer's travel axis and stitched sequentially together, permitted visual upscaling of 2D planar crater profiles into a highly-resolved, 3D space (Fig. 14a, b). The topographic view (Fig. 14a) reveals concentric elevation changes with only minor deviations. In addition, the isometric projection (Fig. 14b) displays smooth gradients with rounded contours, and further confirms final crater axial symmetry. In most cases, final craters exhibited axial symmetry and defined slopes, despite changes in charge size, g-levels, or burial depth. A numerical integration of the 3D crater surface area by a trapezoidal iteration method yields a final crater volume of 419.7 cm^3. The axisymmetric crater profiles in this research indicate that centrifugal air flow, ambient vibrations, and Coriolis effects remain negligible in crater formation within the tested g-level range. To dynamically assess crater stability post-detonation, a compact video camera positioned above the buried charge, monitored final craters in real-time, subsequent blast excavation and centrifuge spin-down. As expected in a granular, cohesionless soil, crater slopes appeared stable with no discernable settling or slumping during centrifuge deceleration.

A quantitative analysis of model-scale final crater dimensions volume V, radius R, and depth H as a function of elevated g-level, for a constant charge size (1 gram) and burial depth (5.1 cm), confirms the previously discussed

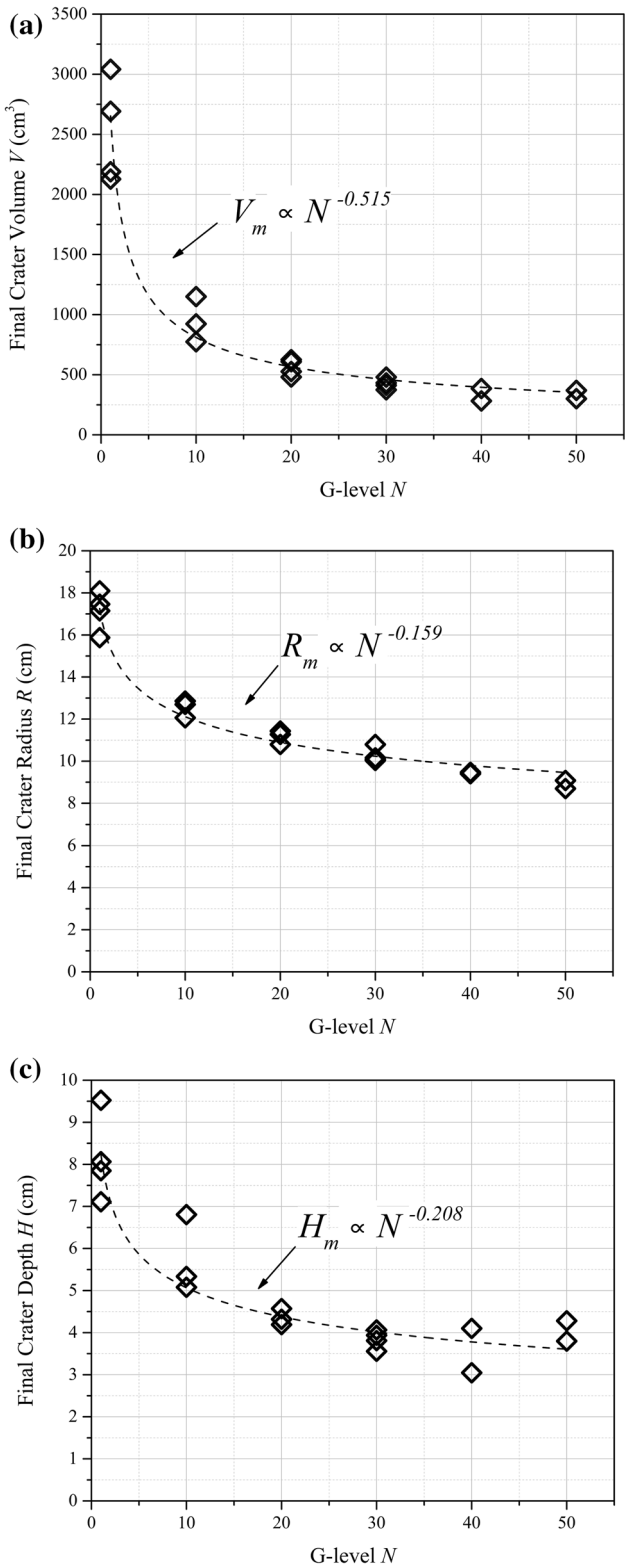

Fig. 15 Model-scale final crater dimensions **a** volume; **b** radius; and **c** depth as a function of g-level subsequent detonation of 1 gram charge buried 5.1 cm. *Dashed-line* represents best-fit derived from power-law regression analysis. Coefficients of determination (R^2) measured: 0.955 (volume), 0.964 (radius), and 0.886 (depth). Plots comprised of seventeen tests

initial vertical soil ejecta velocity trends: gravity-induced confining stresses also significantly impact blast-excavated crater formation. The data again approximates a power-law dependence on g-level as plotted in Fig. 15.

Observed in all three plots, as g-level increases, crater dimensions decrease, indicating a monotonic inverse relationship. Furthermore, final crater measurements evidence considerable repeatability throughout the g-level range tested (Fig. 15). This repeatability, statistically quantified by 95 % confidence intervals (Table 4), shows nominal deviation of final crater measurements from the sample mean and validates test methods. The results demonstrate better reproducibility on the centrifuge when compared to the apparent scatter exhibited in the 1 g-level test series (Fig. 15).

The derived relationships between model final crater dimensions and g-level N are

$$V_m \propto N^{-0.515} \quad (5)$$

$$R_m \propto N^{-0.159} \quad (6)$$

$$H_m \propto N^{-0.208} \quad (7)$$

and demonstrate that final crater dimensions also display a nonlinear reduction subsequent higher gravity-induced stresses. The data again shows a significant decrease between the 1 and 10 g-levels, followed by the expected gradual asymptotic decline.

Mean crater dimensions for the g-level dependent tests (Table 4) include model and prototype scale with uncertainties of two standard deviations. The results show that the maximum model-scale final crater dimensions significantly decrease as a function of gravity-induced overburden stress. Mean final crater volumes decrease 87 % from 1 to 50 g, radius and depth by 48 and 52 %, respectively. The crater parameter depth gradually decreases consequent increased acceleration up to the 30 g-level. At this point, increased gravity appears to have a nominal impact on crater depth. The known sensitivity to confining pressure on the dynamic in-situ shear modulus can explain this observed behavior. The final crater wall angles, defined as $\tan \alpha = H/R$, progressively decrease until the 50 g-level and exhibit an inverse relationship with g-level.

Assuming dynamic similitude and equivalent soil constituent properties, the model-scale charge (1 gram), burial depth (5.1 cm), and crater dimensions extrapolate to prototype conditions via centrifuge scaling relationships as shown Table 4. The results evidence self-consistency and verify the expected trend that charge size and crater dimensions vary proportionally in prototype scale. In a later section, a comparative analysis of this study's empirical scaling relationships to past field tests demonstrates that small-scale laboratory tests using centrifuge scaled modeling simulates larger physical explosive yields.

Table 4 Summary of mean blast-excavated final crater dimensions in model and prototype scale subsequent 1 gram charge buried 5.1 cm and detonated at corresponding g-levels: 1 g, 10 g, 20 g, 30 g, 40 g, and 50 g

G-level N	Mean final crater dimensions								
	Model scale				Prototype scale				
	Radius R (cm)	Depth H (cm)	Volume V (cm^3)	Slope (α)[a] (°)	Charge size (kg)	Burial depth (m)	Radius (m)	Depth (m)	Volume (m^3)
1	17.1 ± 0.92	8.1 ± 0.99	2480.3 ± 425.01	25.3					
10	12.5 ± 0.48	5.7 ± 1.06	932.7 ± 213.87	24.6	1.0	0.51	1.3	0.6	1.1
20	11.0 ± 0.43	4.4 ± 0.21	557.5 ± 66.53	21.8	8.0	1.02	2.2	0.9	4.6
30	10.3 ± 0.52	3.8 ± 0.21	422.2 ± 43.16	20.3	27.0	1.53	3.1	1.1	11.1
40	9.4 ± 0.07	3.8 ± 1.03	351.6 ± 100.94	20.0	64.0	2.04	3.8	1.5	22.7
50	8.9 ± 0.37	3.9 ± 0.47	323.5 ± 66.63	23.7	125.0	2.55	4.5	2.0	42.4

±95 % confidence interval

[a] Slope refers to the crater wall angle with respect to the horizontal

Table 5 Comparison of power–law relationships for model-scale final crater dimensions subsequent centrifuge blast-excavation

	Current study	Schmidt and Holsapple [26]	Goodings et al. [28]
$V_m \propto N^{-\gamma}$, γ	0.515	0.472	0.48
$R_m \propto N^{-\alpha}$, α	0.159	0.159	0.14
$D_m \propto N^{-\beta}$, β	0.208	0.164	0.17

Subscript m stands for model scale; N denotes g-level

Table 5 summarizes the derived power-law exponents relating model-scale final crater dimensions to g-level plotted in Fig. 15. The table also includes the functional relationships between final crater dimensions and gravity reported by Schmidt and Holsapple and Goodings et al. [26, 28].

The power–law relationships for model-scale crater dimensions derived in this study that used fully buried charges, different explosive types and in-situ soil conditions, still demonstrate close agreement to those reported by Schmidt and Holsapple and Goodings et al. [26, 28]. This suggests the absence of gravity related scale effects over a wide range of g-levels (1 g–451 g) and further substantiates the ability of the centrifuge scale modeling technique to alter crater morphology by changing a single parameter: gravity.

A dimensional analysis, performed to better understand the interrelated *physical dynamics* and *statics* intrinsic to soil blast mechanics, correlates initial vertical soil ejecta velocity to blast-excavated crater morphology. The derived dimensionless relationships coupling soil ejecta velocity (v_o) to crater volume (V), radius (R), and depth (H), inclusive of gravity (g), burial depth (D), initial soil density (ρ), and charge mass (W), are represented by the following equations:

$$\frac{v_o}{\sqrt{g}}\left(\frac{\rho}{W}\right)^{1/6} = F_V\left(\frac{V}{D^3}\right)^{m_V} \quad (8)$$

$$\frac{v_o}{\sqrt{g}}\left(\frac{\rho}{W}\right)^{1/6} = F_R\left(\frac{R}{D}\right)^{m_R} \quad (9)$$

$$\frac{v_o}{\sqrt{g}}\left(\frac{\rho}{W}\right)^{1/6} = F_H\left(\frac{H}{D}\right)^{m_H} \quad (10)$$

The coefficients (F) and exponents (m), determined by regression analysis, denote a simple, new coupling function to the specific experimental results. A synthesis of the data for various charge sizes, burial depths, and g-levels, in nondimensional, log–log scale (Fig. 16a–c) adheres best to a power-law fit.

The data clearly shows the expected trend: at a fixed g-level and burial depth, crater dimensions vary proportionally to initial vertical soil ejecta velocities. The self-consistency and similarity in soil behavior between the dynamic and static relationships to the data indicates the suitability of these dimensionless functional relationships (Eqs. 8–10) to physically characterize both soil ejecta velocities and final crater dimensions concisely.

Analysis of Scaling Relationships

The cratering dimensional dependence on explosive mass is analyzed using the empirical cube-root scaling relationship with scaled explosive mass normalized to TNT equivalents [41]. The test parameters include multiple explosive weights (69 mg, 203 mg, 530 mg, and 1 gram),

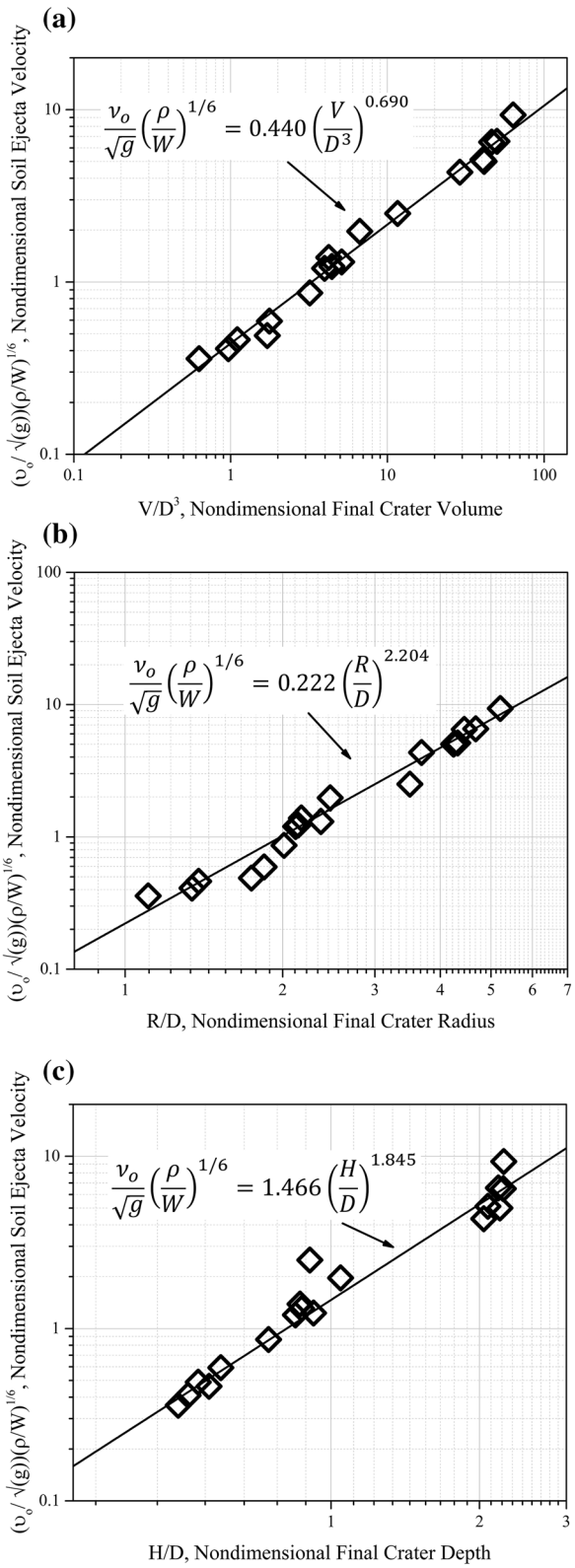

Fig. 16 Dimensionless comparison of initial vertical soil ejecta velocities and final crater dimensions: **a** volume; **b** radius; and **c** depth, for multiple gram-sized charges buried and detonated at various depths and g-levels in logarithmic scale. Best-fit regression lines included (*solid line*)

detonated at varying g-levels (1 g–50 g) under different soil overburdens (1.3 cm–7.6 cm) with soil conditions and explosive type constant.

This study's empirically derived, power-dependent relationships between prototype (p) crater dimensions (meters) and charge weight W (kg) are:

$$V_p \propto W^{0.829} \tag{11}$$

$$R_p \propto W^{0.282} \tag{12}$$

$$H_p \propto W^{0.269} \tag{13}$$

These empirical relationships and this study's data presented in Fig. 17 depict the expected monotonic relationship: crater volume, radius, and depth increase as a function of gravity-scaled explosive mass. Furthermore, to analyze the suitability of conventional cube-root energy scaling methods to predict full-scale crater efficiency, the field test series Erghott, Bergeron et al., and Vortman were selected as a suitable set of comparable data because their works also used fully-buried charges detonated in a dry sand [16, 17, 20]. Rooke et al. field test series were also chosen to compare cratering in moist sand [18].

As shown in all three comparison plots (Fig. 17a–c), this study's results evidence close adherence to the included power-law regression curves, and thus demonstrate self-consistency throughout the range of scaled explosive masses spanning six orders of magnitude. This repeatability, quantified by coefficients of determination (R^2) values (crater volume, radius, and depth: 0.992, 0.993, and 0.978, respectively), indicates nominal variance from the statistical mean.

Furthermore, the cratering dimensional dependence on explosive mass from this study's experimental data in prototype scale displays reasonable agreement to the past field tests (Fig. 17). For example, Vortman detonated 450 kg, 18,143 kg, and 453,000 kg TNT charges in desert alluvium sand and basalt rock [20]. This full-scale test series defines the upper explosive mass limit and yields the maximum final crater dimensions. In spite of geologic differences, excavated crater profiles in desert alluvium soil [20] and bedrock [18] closely approximate this research's regression line. In addition, Erghott [16] and Bergeron et al. [17] used a single charge size (2.27 kg and 100 gram C4, respectively) and their findings correlate reasonably well to this work's mid-range data cluster. The apparent data scatter between the respective field tests and their dissimilarities to this study's results can attribute to differences in explosive mass and chemistry, soil conditions, burial depths, and measurement methods.

The power-dependence on explosive mass derived from this study's experimental data (Eqs. 11–13) is compared to the past centrifuge and field test yield exponents 'n' (Table 6).

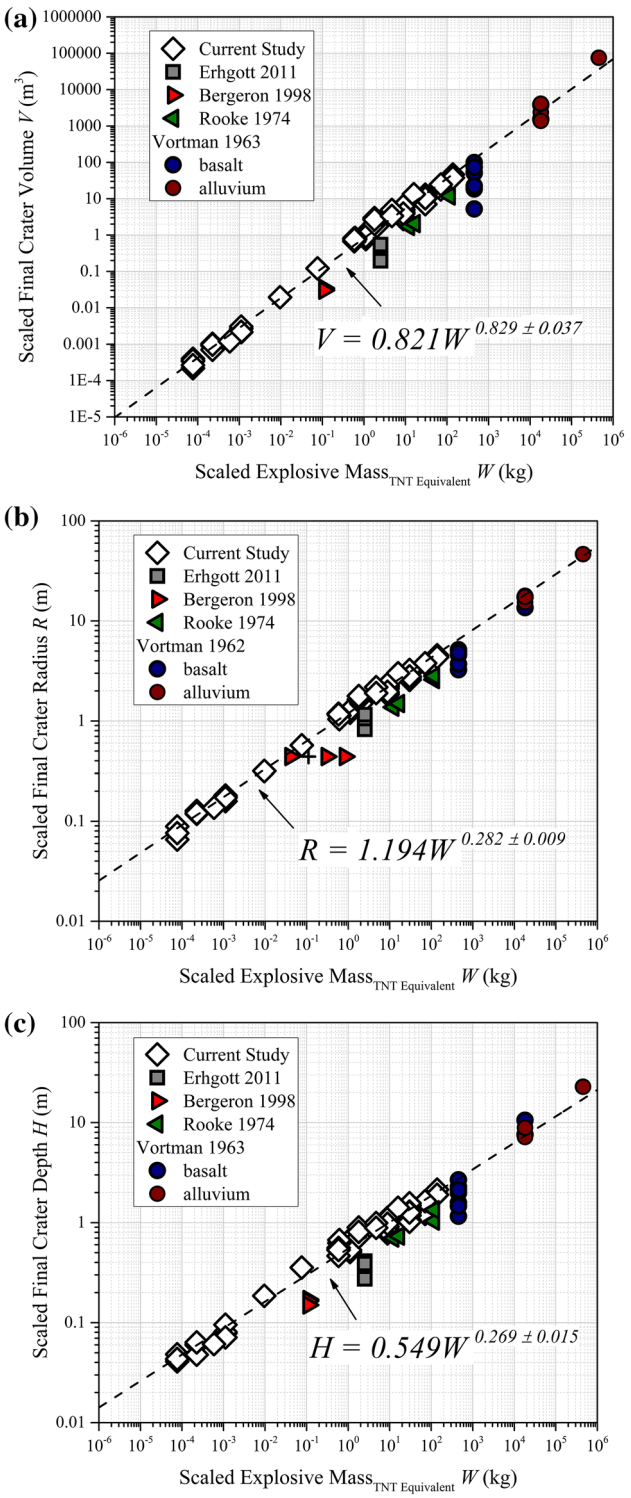

Fig. 17 Comparison of scaled final crater **a** volumes, **b** radii, and **c** depths, as of function of scaled TNT mass equivalent to past larger scale soil blast works plotted in log-log scale. Power-law regression best-fit curves derived from this study's measurements shown as *dashed lines*

Clearly, the conventional method of cube-root energy scaling to predict larger scale yields approximates the cratering phenomenon quite well. However, as shown in Table 6, the cube-root scaling relationships, in all centrifuge studies, underestimate the power-dependence on crater radius and depth. Furthermore, all linear crater dimension exponents appear consistently higher than the quarter-root, gravity scaling method. This research's data indicates that radius and depth power-dependence on the buried charge's weight more closely approximates $W^{1/3.5}$ and $W^{1/3.7}$, respectively, due to the inclusion of lithostatic pressure effects on cratering mechanics.

Next, the dimensionless Π groups are evaluated for performance and applicability to the buried blast cratering phenomena [26, 27]. Their dimensionless crater dependent π terms, or cratering efficiency, are:

$$\pi_V = \frac{V\rho}{W} \tag{14}$$

$$\pi_R = R\left(\frac{\rho}{W}\right)^{\frac{1}{3}} \tag{15}$$

$$\pi_H = H\left(\frac{\rho}{W}\right)^{\frac{1}{3}} \tag{16}$$

where ρ and W denote the initial soil density and charge mass, respectively. In addition, the dimensionless, independent gravity-scaled yield parameter π_2, dependent upon explosive properties, g-level, and charge weight, can be expressed as

$$\pi_2 = \left(\frac{g}{Q}\right)\left(\frac{W}{\delta}\right)^{1/3} \tag{17}$$

where g denotes g-level; Q and δ represent the explosive's specific heat and density, respectively. This π group enables comparisons of non-similar experiments to different scaled yields for a given charge size and explosive type. This study's data in dimensionless form demonstrates reasonable adherence to a power-law fit as shown in Fig. 18. The empirical relationship reveals the expected inverse proportionality: as gravity scaled yield (π_2) increases, volume cratering efficiency (π_V) decreases.

The two power-law regression curves appear nearly parallel, substantiated by the closeness of the power exponents: −0.489 and −0.482 for the 2.5 cm and 5.1 cm burial depths, respectively. The 2.5 cm DOB data line represents the highest volume cratering efficiency for all values of π_2, and the deeper 5.1 cm DOB corresponds to lower cratering efficiency values. This trend continues with the deepest 7.6 cm burial depth equating to the lowest crater volume efficiencies for $\pi_2 = 2.5E{-}10$ and

Table 6 Comparison of scaled yield exponent, n, for buried blasts in soil

	Current study[a]	Brownell et. al. [29][a]	Goodings et. al. [28][a]	Schmidt et al. [26][a]	Rooke et al. [18][b]	Vortman [20][b]	
	Mason sand, dry	Beach sand, dry	Ottawa sand, dry	Ottawa sand, dry	Sand, moist	Basalt, dry	Alluvium, dry
$V_p \propto W^n$	0.829	0.831	0.84	0.842	0.874	1.018	1.072
$R_p \propto W^n$	0.282	0.297	0.29	0.280	0.302	0.305	0.317
$H_p \propto W^n$	0.269	0.279	0.28	0.279	0.237	0.381	0.326

Subscript p stands for prototype; Test environment: [a] Centrifuge; [b] Field

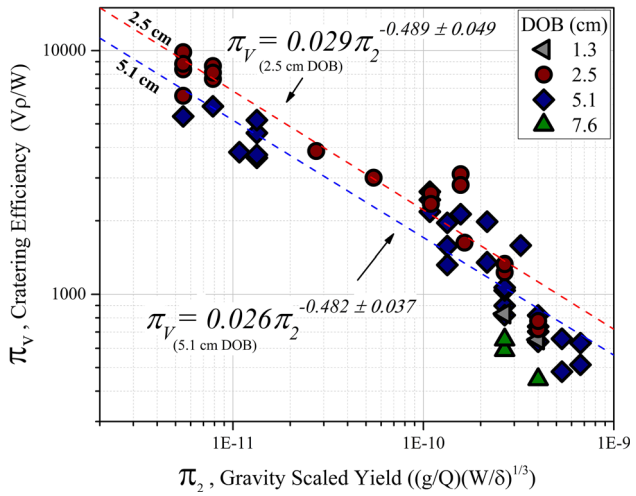

Fig. 18 Volume crater efficiency π_V as a function of gravity scaled yield π_2 in log–log scale. Data corresponds to buried charge detonations of various charge sizes at multiple g-levels. Power-law regression curves included (*dashed lines*) for burial depths 2.5 cm ($R^2 = 0.924$) and 5.1 cm ($R^2 = 0.863$). For all tests, $\delta = 1770$ kg/m^3 and $Q = 6.19 \times 10^6$ m^2/s^2

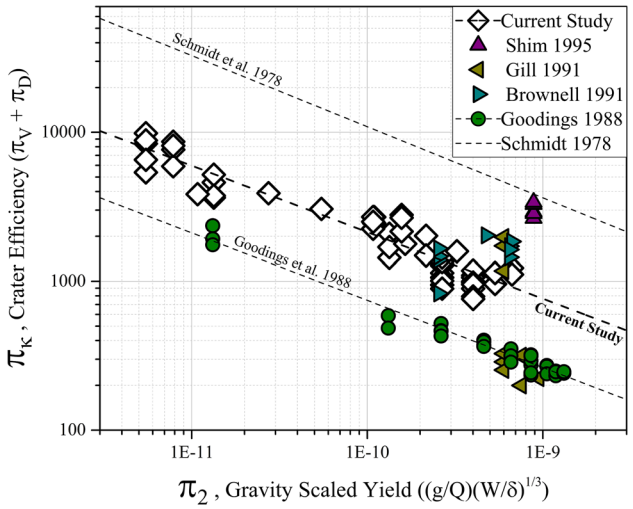

Fig. 19 Comparison of volume cratering efficiency π_K as a function of π_2 in log–log scale for multiple centrifuge soil blast studies. *Dashed lines* indicate power–law regression curves

$\pi_2 = 4E{-}10$. The soil behavior can attribute to the gravity-induced increase in shear strength consequent matrix stiffening which inhibits crater volume expansion. Note that the shallowest burial depth (1.3 cm) and equivalent $\pi_2 = 2.5E{-}10$ and $\pi_2 = 4E{-}10$, π_V shows intermediate values relative to the 2.5 cm and 5.1 cm burial depths and indicates that the crater efficiency dependence on burial depth is not monotonic. The DOB can be altered to optimize the volume of soil ejected from the crater with resultant increased cratering efficiency [24, 42]. The self-consistency observed in the examined gravity scaled yield regime suggests negligible adverse scaling effects and the relevance of the dimensionless π_2 parameter.

Table 7 summarizes the power-law exponents (α) and constants (c) derived from a regression analysis of the 2.5 cm and 5.1 cm burial depth results (Fig. 18) and includes the experimentally determined π relationships reported by Schmidt and Holsapple [26] and Goodings et al. [28].

In all three studies, the crater dependent yield exponents demonstrate close correspondence and thus indicate similar

Table 7 Comparison of the π-group first order, least-square fit parameters α and c

	Current study				Schmidt and Holsapple [26]		Goodings et al. [28]	
	2.5 cm DOB		5.1 cm DOB		Half-buried		Half-buried	
	α	c	α	c	α	c	α	c
$\pi_v\pi_2^\alpha = c$	0.489	0.029	0.482	0.026	0.472	0.194	0.452	0.023
$\pi_r\pi_2^\alpha = c$	0.166	0.351	0.143	0.575	0.159	0.765	0.147	0.409
$\pi_h\pi_2^\alpha = c$	0.158	0.222	0.196	0.074	0.164	0.154	0.220	0.023

soil blast mechanics and consequent crater formation despite varying test parameters, specifically lithostatic pressure, which can explain the variation between the exponents reported in this study compared to Schmidt and Holsapple [26] and Goodings et al. [28].

The previous dimensionless analysis of the classical Π term relationships derived for surface-tangent burst in past studies (Table 7) compared favorably to this work's empirical relationships and further confirms the suitability of the Π terms to simulate larger explosive yields. Here, a new dimensionless parameter, π_κ, written in the form

$$\pi_\kappa = \pi_V + \pi_D \tag{18}$$

refines the volume cratering efficiency parameter, π_V (Eq. 14), to incorporate soil overburden effects through inclusion of a constituent term, π_D, defined as

$$\pi_D = N\left(\frac{D}{a_W}\right) \tag{19}$$

The addition of the gravity scale factor, N, explosive diameter, a_W, and burial depth, D, a key parameter in the dimensionless analysis, allows an enhanced characterization of sub-surface detonations at elevated gravity. For surface blast excavations, the classical volume cratering efficiency term, π_V, remains unchanged, as π_D equals zero and π_κ simplifies to π_V. An empirical relationship between π_κ and π_2, derived from a power-law regression fit to this study's empirical data, approximates the following equation:

$$\pi_\kappa \pi_2^{0.446} = 0.074 \tag{20}$$

The power–law relationships, summarized in Table 7, in conjunction with and the new dimensionless term, π_κ (Eq. 20), are plotted in Fig. 19 which now includes the data reported by Brownell and Charlie [29], Gill and Kuennen [30], and Shim [31].

The comparison plot (Fig. 19) depicts this compilation of centrifuge soil blast data extending roughly four orders of magnitude of gravity-scaled yields. In general, the data shows progressively smaller values of π_κ as π_2 increases, consistent with the cratering efficiency dependent trend characterized in Fig. 18. As anticipated, due to the close correspondence evidenced in the power-law exponents (Table 7), the Schmidt and Holsapple [26] and Goodings et al. [28] best fit lines appear nearly parallel to this study's regression curve. However, the Schmidt and Holsapple line corresponds to higher crater efficiencies for equivalent gravity-scaled yields when compared to all the other represented centrifuge studies. This can attribute to the higher g-levels and charge sizes included in their π_2 calculations as well as differences in their soil's unit weight. Gill and Kuennen [30] also measured blast excavated craters in a dry soil using surface-tangent charges and three subsurface charges. Their subsurface tests are in close agreement to this study's data, reflecting similar DOBs and g-levels. Similarly, the dry sand crater efficiencies reported by Brownell and Charlie [29] remain coincident to this study's regression line. However, the matrix suction in their partially saturated soil induced slightly higher crater efficiencies relative to this study. Moreover, Shim [31] reported that final crater dimensions measured greater in a saturated soil, hence, their volume cratering efficiencies remain consistently higher when compared to this research. The new π_κ term refines the classical π_V parameter to include lithostatic effects and provides direct comparisons across studies of different material types and test configurations.

Conclusions

This comprehensive experimental regime augments the current literature by quantifying the buried, explosive-induced, high-rate soil ejecta kinematics in conjunction with crater morphology, using state-of-the-art technologies and novel measurement methodologies that improved data resolution and accuracy. The empirical relationships demonstrate a gravity-dependent reduction in the temporal and spatial ejecta flow and also blast-excavated crater dimensions. The in-depth analysis of this study's data in both dimensional and dimensionless form compared favorably to a compilation of past field and centrifuge results across a wide range of material types and test configurations. This further confirms that centrifuge modeling enables small, gram-sized charges to simulate blast energy typical of a full-scale field test. In addition, the highly-resolved, rate-dependent, video images enhanced the understanding of the complex, interactive soil blast mechanisms and simulate the same phenomenon evident in full-scale blast events. Therefore, they provide a sound physical basis for multiphasic computational models of the dynamic mechanical material response with identification of initial soil deformation and subsequent soil ejecta flow. Furthermore, the repeatable, high-fidelity experimental database allows parametric calibration and stringent validation for advanced numerical simulations of soil blast mechanics and contributes to the development of protective armoring technologies for military personnel and vehicles.

The versatile experimental platform readily adapts to different parametric investigation of soil blast mechanics: different soil types (cohesive and cohesionless), moisture content (dry to partially saturated and full saturated) with in-situ material variations; charge explosive mass; burial depths; and g-levels. Importantly, the new measurement methodologies have potential applications to extended fields of geomechanics, such as impact cratering, soil–

structure interaction including blast impact on an overlying target, earthquake simulations, and forensic engineering identification of material deformation and failure. This research advances the current understanding of buried, blast-induced soil mechanics rendering it a truly adaptive technological platform.

Acknowledgments The authors would like to thank the following individuals: William Cooper of the Air Force Research Laboratory (Kirtland, NM) for his expertise and participation in this investigation; Pierce Jarrell and Tyler Leigh for their laboratory assistance and data compilation. Funding for this research provided by an Office of Naval Research MURI Grant N00014-11-1-0691 is gratefully acknowledged.

Appendix

See Table 8.

Table 8 Scaling relationships for dynamic centrifuge tests

Quantity	Prototype	Model at *Ng*
Length	N	1
Time (dynamic)	N	1
Area	N^2	1
Volume	N^3	1
Velocity	1	1
Acceleration	1	N
Mass	N^3	1
Force	N^2	1
Stress	1	1
Energy	N^3	1

References

1. Runciman N, Vagenas N (1998) Evaluation of underground drill and blast mining systems using discrete-event simulation. Miner Resour Eng 7:211–220
2. Ashford SA, Rollins KM, Lane JD (2004) Blast-induced liquefaction for full-scale foundation testing. J Geotech Geoenviron Eng 130:798–806
3. Housen KR, Holsapple KA (2011) Ejecta from impact craters. Icarus 211:856–875
4. Goodings DJ, Lin C-P, Dick RD et al (1992) Modeling effects of chemical explosives for excavation on moon. J Aerosp Eng 5:44–58
5. Gault DE, Wedekind JA (1978) Experimental studies of oblique impact. In: Lunar Planet. Science Conference Proceeding, pp 3843–3875
6. Wünnemann K, Nowka D, Collins GS et al (2011) Scaling of impact crater formation on planetary surfaces: Insights from numerical modeling. In: Proceedings of 11th hypervelocity impact symposium, pp 1–16
7. Bull JW, Woodford CH (1998) Camouflets and their effect on runway support. Comput Struct 69:695–706
8. Kutter BL, O'Leary LM, Thompson PY, Lather R (1988) Gravity-scaled tests on blast-induced soil–structure interaction. J Geotech Eng 114:431–447
9. Anirban D, Thomas FZ (2007) Centrifuge modeling of surface blast effects on underground structures. Geotech Test J 30:1–5
10. Tabatabai H, Bloomquist D, McVay MC et al (1988) Centrifugal modeling of underground structures subjected to blast loading. Department of Civil and Coastal Engineering, University of Florida, Gainesville
11. Parkes J, Kelly H, Munfakh G, Choi S (2013) Analyzing the impacts of explosions on dams and levees. Saf Secur Eng V 134:307
12. Sharp MK, Matheu E, Seda-Sanabria Y (2011) Blast damage assessment and mitigation for dams and navigation locks. Risk Anal Dam Saf Dam Secur Crit Infrastruct Manag 381
13. Wu C, Hao H, Lu Y, Sun S (2004) Numerical simulation of structural responses on a sand layer to blast induced ground excitations. Comput Struct 82:799–814
14. Roy PP (1998) Technical note characteristics of ground vibrations and structural response to surface and underground blasting. Geotech Geol Eng 16:151–166
15. Bleiweis PB, Hart GC, Smith CB, Matthiesen RB (1973) Simulation of strong motion earthquake effects on structures using explosive blasts. Nucl Eng Des 25:126–149
16. Ehrgott JQ Jr (2010) Influence of soil properties on the aboveground blast environment from a near-surface detonation. Ph.D., Mississippi State University
17. Defence Research Establishment Suffield, Coffey C, Walker R, Bergeron D (1998) Detonation of 100-gram anti-personnel mine surrogate charges in sand a test case for computer code validation. Defence Research Establishment Suffield [Medicine Hat, AB]
18. Rooke AD, Carnes BL, Davis LK (1974) Cratering by explosions: a compendium and an analysis. Waterways Experiment Station
19. Drake JL, Little CD, MS AEWESV (1983) Ground shock from penetrating conventional weapons. Defense Technical Information Center
20. Vortman IJ (1963) Cratering experiments with large high-explosive charges. Geophysics 28:351–368
21. Fox DM, Huang X, Jung D et al (2011) The response of small scale rigid targets to shallow buried explosive detonations. Int J Impact Eng 38:882–891. doi:10.1016/j.ijimpeng.2011.05.009
22. Genson K (2006) Vehicle shaping for mine blast damage reduction. MS Thesis, Maryland
23. Fourney WL, Leiste U, Bonenberger R, Goodings DJ (2005) Mechanism of loading on plates due to explosive detonation. Fragblast 9:205–217. doi:10.1080/13855140500431989
24. Johnson SW, Smith JA, Franklin EG et al (1969) Gravity and atmospheric pressure effects on crater formation in sand. J Geophys Res 74:4838–4850. doi:10.1029/JB074i020p04838
25. Chabai AJ (1965) On scaling dimensions of craters produced by buried explosives. J Geophys Res 70:5075–5098. doi:10.1029/JZ070i020p05075
26. Schmidt R, Holsapple K (1978) Centrifuge cratering scaling experiment I: dry granular soils. Boeing Aerosp, Co
27. Schmidt RM, Holsapple KA (1980) Theory and experiments on centrifuge cratering. J Geophys Res Solid Earth 85:235–252. doi:10.1029/JB085iB01p00235
28. Goodings DJ, Fourney WL, Dick RD (1988) Geotechnical centrifuge modeling of explosion induced craters—a check for scaling effects. DTIC Document

29. Brownell KC, Charlie WA (1992) Centrifuge modeling of explosion-induced craters in unsaturated sand. DTIC Document
30. Gill JJ, Kuennen ST (1991) Half-space modeling of explosively-formed craters. In: Proceedings of international conference centrifuge, pp 465–472
31. Shim H (1995) Response of piles in saturated soil under blast loading. Ph.D. Thesis, Colorado
32. Davies MCR (1994) Dynamic soil structure interaction resulting from blast loading. Leung Lee Tan Eds Centrif 94:319–324
33. Lenke LR, Pak RY, Ko H-Y (1991) Boundary effects in modeling of foundations subjected to vertical excitation. In: Centrifuge, pp 473–480
34. Pak RY, Guzina BB (1995) Dynamic characterization of vertically loaded foundations on granular soils. J Geotech Eng 121:274–286
35. Pak RYS, Soudkhah M, Abedzadeh F (2011) Experimental synthesis of seismic horizontal free-field motion of soil in finite-domain simulations with absorbing boundary. Soil Dyn Earthq Eng 31:1529–1539. doi:10.1016/j.soildyn.2011.06.002
36. Svoboda J (2013) Impact of strain rate on the shear strength and pore water pressure generation of clays and sands. University of Colorado at Boulder
37. Svoboda JS, McCartney JS (2014) Shearing rate effects on dense sand and compacted clay. In: Dyn Behav Mater, volume 1. Springer, Berlin, pp 389–395
38. Taylor LC, Fourney WL, Leiste U, Cheeseman BA (2008) Loading mechanisms on a target from detonation of a buried charge. 24th international symposium Ballist. p 1
39. Bergeron D, Tremblay JE (2000) Canadian research to characterize mine blast output. 16th international MABS symposium
40. Vision Research Digital High-Speed Cameras Measuring Motion with Imaging Software. https://www.highspeedcameras.com/Solutions/Common-Applications/Motion-Analysis. Accessed 19 Mar 2016
41. Cooper P (1996) Explosives engineering, 1st edn. Wiley-VCH, New York
42. NATO (2004) Test methodologies for personal protective equipment against anti-personnel mine blast. France